4

Continuum Mechanics of Solid Oxide Fuel Cells Using Three-Dimensional Reconstructed Microstructures

Sushrut Vaidya and Jeong-Ho Kim*
Department of Civil and Environmental Engineering, University of Connecticut, USA

1. Introduction

A solid oxide fuel cell (SOFC) is a device that converts the chemical energy of fuels into electrical energy (Singhal & Kendall, 2003). SOFCs have received much attention from researchers due to their promise of delivering relatively clean energy at high efficiencies (Singhal & Kendall, 2003). An SOFC consists of a few basic parts: an anode, a cathode, an electrolyte, and interconnect wires (Singhal & Kendall, 2003). The electrolyte in an SOFC is a solid oxide such as Yttria-Stabilized Zirconia (YSZ). The porous anode is usually a ceramic-metal composite (so called cermet) such as the nickel-zirconia cermet (Ni-YSZ). The porous cathode is usually a composite of strontium-doped lanthanum manganite (LSM) and Yttria-Stabilized Zirconia (LSM-YSZ) (Singhal & Kendall, 2003) or a composite such as gadolinium-doped ceria-lanthanum strontium cobalt ferrite (GDC-LSCF) (Anandakumar et al., 2010). Oxygen atoms undergo reduction on the porous cathode surface, and the resulting oxide ions are transported through the electrolyte to the porous anode. Here, the oxide ions react with the fuel (such as hydrogen). Hydrogen is oxidized, and the electrons of the oxide ions are liberated. The free electrons give rise to electric current (Singhal & Kendall, 2003).

Research on SOFCs has concentrated on many different aspects, including anode, cathode, and electrolyte materials; investigating the behavior of different SOFC configurations; modeling and simulating electrochemical, thermal, and flow phenomena; and performing thermal stress and probability of failure analyses. Researchers have employed experimental, analytical, and computational approaches in their investigations. For example, Selcuk and Atkinson (1997, 2000) conducted a number of experimental studies to estimate various mechanical properties of SOFC ceramic materials such as YSZ and NiO-YSZ. They determined the biaxial flexural strength and fracture toughness of YSZ both at room temperature and an operating temperature of 900^0C (Selcuk & Atkinson, 2000). They also experimentally studied the dependence of the Young's modulus, shear modulus, and Poisson's ratio of YSZ and NiO-YSZ (amongst other ceramic materials) on porosity (Selcuk & Atkinson, 1997). The results of these studies were summarized by the authors (Atkinson & Selcuk, 2000) where they also suggested techniques for improving the mechanical

* Corresponding Author

behavior of SOFC ceramic materials under certain operating conditions. Toftegaard et al. (2009) conducted uniaxial tensile tests on pure YSZ specimens and YSZ specimens coated with porous NiO-YSZ layers. They heat-treated the coated YSZ specimens at various temperatures to study the effect of heat treatment at different temperatures on the strength. Pihlatie et al. (2009) experimentally determined the Young's modulus (amongst other mechanical properties) of Ni-YSZ and NiO-YSZ composites as a function of porosity using the Impulse Excitation Technique (IET). They also used IET to study the dependency of the Young's modulus of these materials on temperature. Giraud and Canel (2008) also conducted experimental studies using IET to determine the variation of the Young's modulus of YSZ, LSM, and Ni-YSZ with temperature. Wilson and Barnett (2008) conducted experimental studies on Ni-YSZ/YSZ/LSM-YSZ SOFCs with Ni-YSZ anodes of different compositions to investigate the effect of varying composition of the anodes on their performance and microstructure. Their studies involved serial-sectioning using a focused ion beam scanning electron microscope (FIB-SEM) to obtain images of the microstructures of the different samples. They conducted stereological analyses on these images to calculate volume fractions and triple-phase boundary (TPB) densities for their samples. Zhang et al. (2008) proposed an analytical model for calculating residual stresses in a single SOFC with NiO-YSZ/YSZ/LSM composition. They used their model to estimate the residual stresses in an SOFC at room temperature and to study the variation of the stresses in the different components with changes in component thicknesses. They also carried out a Weibull analysis to calculate the probability of failure of the anode, and they studied the variation of the failure probability of the anode with changes in component thicknesses.

Laurencin et al. (2008) have proposed a numerical (finite element analysis-based) tool for studying the degradation of anode-supported and electrolyte-supported planar SOFCs under several types of mechanical loads, including residual stresses. They have also calculated the failure probabilities of the SOFCs using Weibull analysis. Pitakthapanaphong and Busso (2005) carried out finite element analyses to investigate the fracture of multi-layered systems used in SOFCs, such as LSM films on a YSZ substrate. They have pointed out that fracture is caused by large residual stresses induced during the SOFC manufacturing process due to thermal expansion coefficient (TEC) mismatch between different layers. They observed different cracking patterns (surface cracks, channeling cracks, and interfacial cracks) in physical samples of multi-layered systems. Their study involved FE simulations to determine the crack driving force (energy release rate) for the three observed cracking patterns. Johnson and Qu (2008) used a three-dimensional stochastic reconstruction method to create multiple realizations of the microstructure of porous Ni-YSZ cermet used as SOFC anode material. They analyzed these microstructure realizations using finite element software to determine the effective elastic modulus and effective coefficient of thermal expansion (CTE) of Ni-YSZ as a function of temperature. Anandakumar et al. (2010) carried out FE analyses to estimate thermal stresses and probability of failure in functionally graded SOFCs. They employed a continuum mechanics approach and used graded finite elements to discretize effective media consisting of NiO-YSZ/YSZ/LSM as well as NiO-YSZ/YSZ/GDC-LSCF. They used the Weibull method to determine the failure probability of the individual components of the SOFC, as well as the failure probability of the whole SOFC. They found that the thermal stresses developed in functionally graded SOFCs under spatially uniform and non-uniform temperature loads are

lower than those induced in conventional layered SOFCs. They also found that functionally graded SOFCs show a lower probability of failure than other types of SOFCs.

In this work, three-dimensional micromechanical finite element (FE) models for real solid oxide fuel cell (SOFC) anode and cathode microstructures are generated from a stack of two-dimensional image-based FE models of anode and cathode microstructures. Finite element analysis (FEA) of the models is carried out to determine their mechanical response to a steady-state temperature change from room temperature up to an operating temperature. The resulting stress distribution is determined in each case, and the stresses are analyzed using the Weibull method to calculate the probability of failure. The anode material is Ni-YSZ, while the cathode material is LSM-YSZ. Both linear elastic and elastic-plastic (nonlinear) behaviors are considered for nickel in the analysis of the anode. It is observed that the linear elastic models underestimate the probability of failure of the anode. The effect of temperature-dependent material properties on the probability of failure of the anode and cathode is also investigated. *The novelties of this work include micromechanical finite element analysis of the mechanical response of anode and cathode microstructural models considering temperature-dependent material properties and nonlinear elastic-plastic behavior of the nickel phase.*

2. Image-based microstructural finite element models

The first step in this work was to digitally reconstruct a three-dimensional (3-D) anode microstructure from two-dimensional (2-D) images of anode cross-sections obtained using focused ion beam-scanning electron microscopy (FIB-SEM). The 2-D images of the anode and cathode microstructures were obtained from Dr. Scott Barnett's research group at Northwestern University (Wilson et al., 2006, 2009). The initial 3-D reconstruction was achieved using IMOD (Kramer et al., 1996), a free collection of image processing programs developed by scientists at the Boulder Laboratory for 3-D Electron Microscopy of Cells. IMOD is capable of creating a stack of 2-D images, interpolating the gaps between consecutive images, and creating and displaying the 3-D model. A few representative 2-D images and the 3-D reconstruction of the anode microstructure are shown in Figure 1. The in-plane dimensions of the reconstructed anode are 5 μm x 6 μm, while the thickness is 3.54 μm.

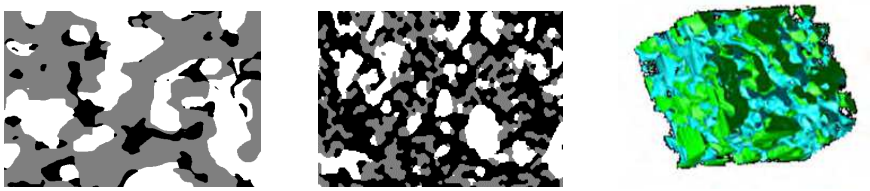

Fig. 1. Two-dimensional SEM images of anode (left) and cathode (center) cross-sections (Wilson et al., 2006, 2009) and a reconstructed three-dimensional anode (right)

In the SEM images of the anode, white (pixel value 255) corresponds to nickel, gray (pixel value 127) to YSZ, and black (pixel value 0) to the pores. In the images of the cathode, white (pixel value 255) represents LSM, gray (pixel value 127) represents YSZ, and black (pixel value 0) represents the pores. The reconstructed 3-D model was used as a check on the geometry of the 3-D FE model.

The next step involved the creation of a single 2-D FE model from a single 2-D SEM image. FE modeling was carried out using the commercial FE software ABAQUS v6.9 (Dassault Systems Simulia Corp., Providence, Rhode Island, USA). This was done by writing a MATLAB ® program (R2010a, The MathWorks, Inc., Natick, Massachusetts, USA) to recreate the geometry of the image using 2-D finite elements (4-node quadrilateral elements) and write the geometry data to an ABAQUS input file. Exactly one element was assigned to each pixel in the image, and the element was assigned to the appropriate element set (nickel or YSZ) based on the pixel value. Information concerning the material properties, boundary conditions, initial temperature, temperature field, and required outputs (e.g. principal stresses) was also specified in the input file. The input file was then run using ABAQUS to generate the 2-D FE model as shown in Figure 2.

Fig. 2. Two-dimensional FE model of a single cross-section of the SOFC anode

The 3-D FE anode and cathode models were created by making a stack of all the 2-D images and introducing a "buffer" plane between each pair of consecutive images. This was necessary and useful to ensure a simple step variation in material properties between corresponding regions in two consecutive images. Then the gaps between consecutive images were interpolated by assigning one three-dimensional 8-node brick element to each volumetric pixel (or voxel). Thus, the 3-D geometries of the anode and cathode microstructures were recreated in the 3-D FE models of the anode and cathode. Various free-body cuts of the 3-D FE anode model are shown in Figure 3.

Fig. 3. Free-body cuts of the three-dimensional FE model of the SOFC anode

3. Finite element analysis of anode and cathode models

3.1 Analysis models and metrics

The FE analysis of the anode and cathode models was carried out to investigate the effect of various temperature loads, as well as the effect of variation of material properties with temperature, on the mechanical response and probability of failure. In the case of the anode, the effect of nonlinear (elastic-plastic) behavior versus linear elastic behavior of nickel was also investigated, which has not been studied in the literature.

The FE analyses of the anode and cathode models were divided into different categories as explained in Tables 1 and 2. In each case, the FE model was subjected to fixed boundary conditions (i.e. all nodes on each of the six faces were allowed neither to translate nor to rotate). The behavior of the model with increasing temperature loads was investigated by subjecting the model to eight different spatially uniform predefined temperature fields of magnitude 120^0C, 220^0C, 320^0C, ..., 820^0C. In each analysis, the initial temperature was specified as 20^0C (room temperature), so that the model was subjected to eight different magnitudes of temperature change ($\Delta T = 100^0$C, 200^0C, 300^0C, ..., 800^0C)..

Case	Ni	YSZ	Temperature-dependence (Ni)	Temperature-dependence (YSZ)
Case 1: Temperature-independent	Linear elastic	Linear elastic	None	None
Case 2: Temperature-dependent CTEs	Linear elastic	Linear elastic	CTE	CTE
Case 3: Elastic-plastic behavior of Ni	Elastic-plastic	Linear elastic	CTE	Young's modulus, CTE

Table 1. Metrics for finite element analyses of anode

Case	LSM	YSZ	Temperature-dependence (LSM)	Temperature-dependence (YSZ)
Case 1: Temperature-independent	Linear elastic	Linear elastic	None	None
Case 2: Temperature-dependent	Linear elastic	Linear elastic	Young's modulus	Young's modulus, CTE

Table 2. Metrics for finite element analyses of cathode

3.2 Material properties

Table 3 lists the room temperature material properties used for nickel, YSZ and LSM (Johnson & Qu, 2008; Anandakumar et al., 2010).

Material	Young's modulus (GPa)	Poisson's ratio	CTE (10^{-6} ^{0}C^{-1})
Nickel	207	0.31	12.50
YSZ	205	0.30	10.40
LSM	40	0.25	11.40

Table 3. Room temperature material properties used in FE analyses

Figure 4 shows the variation of the coefficients of thermal expansion of nickel and YSZ with temperature (Johnson & Qu, 2008). The CTE of LSM was assumed to be constant over the temperature range considered. The room temperature value of the CTE of LSM (as shown in Table 3) was used in the FE analyses of the cathode.

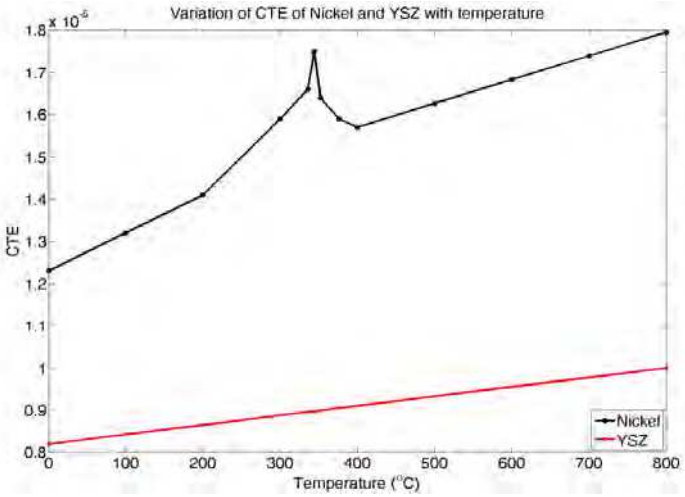

Fig. 4. Variation of CTE of nickel and YSZ with temperature (Johnson & Qu, 2008).

Figure 5 shows the variation of the Young's modulus of LSM and YSZ with temperature (Giraud & Canel, 2008). The Young's modulus of nickel was assumed to be constant over the temperature range considered. The room temperature value of the Young's modulus of nickel (as shown in Table 3) was used in the FE analyses of the anode.

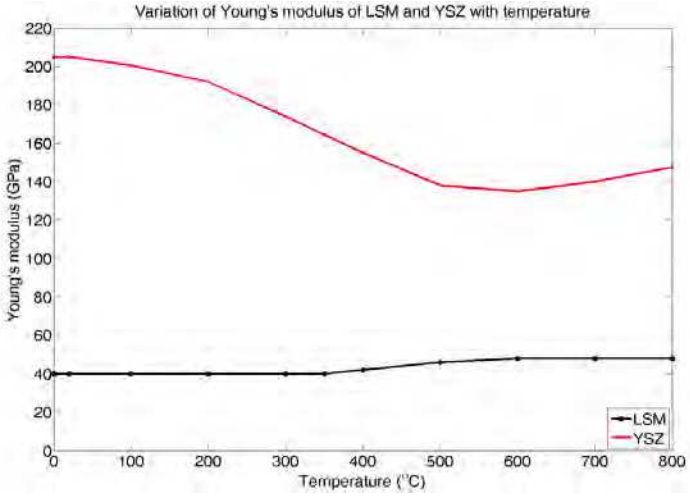

Fig. 5. Variation of Young's modulus of LSM and YSZ with temperature (Giraud and Canel, 2008).

Figure 6 shows the stress-strain curve used to describe the elastic-plastic behavior of nickel (Ebrahimi et al., 1999). It was assumed in this work that the stress-strain curve of nickel does not change over the temperature range considered.

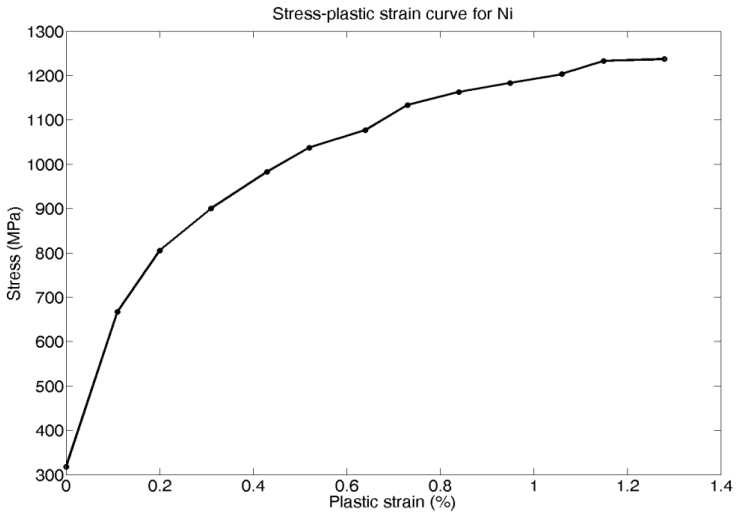

Fig. 6. Stress-plastic strain curve for nickel (Ebrahimi et al., 1999).

4. Finite element analysis results and discussion

4.1 Stress analysis

The full 3-D FE models of the anode (50:50 NiO:YSZ weight percentage composition) and cathode (50:50 LSM:YSZ weight percentage composition) are shown in Figure 7. The FE anode model consists of 406,465 elements and 473,181 nodes. The cathode model has 244,584 elements and 395,131 nodes.

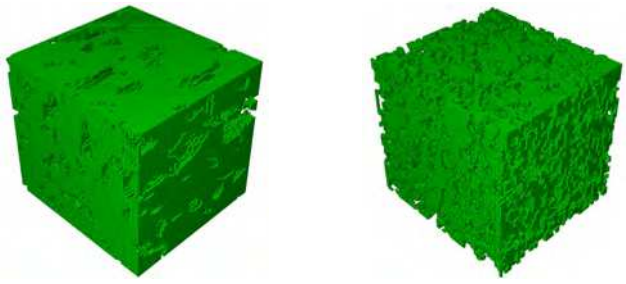

Fig. 7. Three-dimensional FE models of anode (left) and cathode (right)

4.1.1 Anode microstructure

The von Mises stress contour plots for the anode at $\Delta T = 100^0C$, 500^0C, and 800^0C are shown considering elastic-plastic behavior of nickel in Figure 8. The stress values are in units of N/m^2 (i.e., Pa).

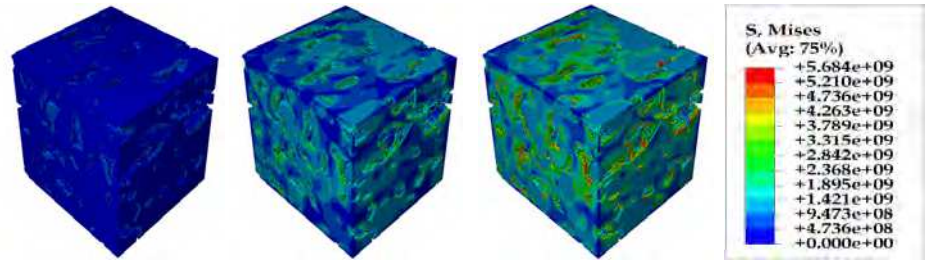

Fig. 8. Von Mises stress contour plots for anode considering elastic-plastic behavior of nickel: (left to right) $\Delta T = 100^0C$, $\Delta T = 500^0C$, $\Delta T = 800^0C$

Figure 8 shows that as ΔT increases from 100ºC to 800ºC, the stresses in the anode also increase. This happens because thermal stress is proportional to the CTE, and the CTEs of both nickel and YSZ increase with temperature, as seen from Figure 4. Also, the stress plots show that the stresses are greater near the regions of pores due to stress concentration, as expected. Similar results are obtained for the cases with temperature-independent material properties and temperature-dependent CTEs. The effect of the elastic-plastic behavior of nickel on the principal tensile stress values (as compared with the linear elastic behavior assumed in the cases with temperature-independent material properties and temperature-dependent CTEs) is discussed in section 4.2.1, which deals with failure probability calculations for the anode.

4.1.2 Cathode microstructure

The von Mises stress contour plots for the cathode at ΔT = 100ºC, 500ºC, and 800ºC are shown in Figure 9 considering temperature-dependent material properties.

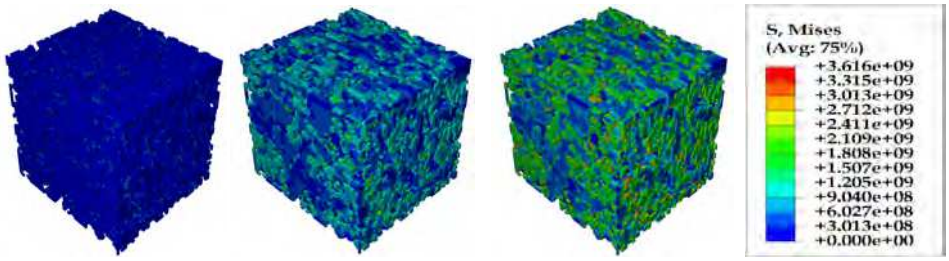

Fig. 9. Von Mises stress contour plots for cathode considering temperature-dependent material properties: (left to right) $\Delta T = 100^0C$, $\Delta T = 500^0C$, $\Delta T = 800^0C$

Figure 9 shows that as ΔT increases from 100^0C to 800^0C, the stresses in the cathode also increase. This result can be explained, just as in the case of the anode, by the fact that thermal stress is proportional to the CTE, and the CTE of YSZ increases with temperature while the CTE of LSM is assumed constant over the temperature range considered. Also, the plots show that the stresses are greater near the regions of pores due to stress concentration. Similar results were obtained for the case with temperature-independent material properties. The effect of temperature-independent versus temperature-dependent material properties on the principal tensile stresses induced in the cathode is discussed in section 4.2.2, which deals with failure probability calculations for the cathode.

4.2 Probability of failure analysis

Ceramic materials exhibit brittle behavior under tensile stress. Also, unlike metals, they show wide variability in tensile strength values and follow a statistical strength distribution. Thus, the Weibull method of analysis (Weibull, 1951; Laurencin et al., 2008) was used to calculate the probability of failure of each SOFC component (anode/cathode). According to the Weibull method, the survival probability of a particular component j under the action of a tensile stress σ is given by (Laurencin et al., 2008):

$$P_s^j\left(\sigma, V_j\right) = \exp\left(-\int_{V_j}\left(\frac{\sigma}{\sigma_0}\right)^m \frac{dV_j}{V_0}\right) \tag{1}$$

where j = anode or cathode, V_j is the volume of component j, V_0 is a characteristic specimen volume (reference volume) for the material of component j, σ_0 is the characteristic strength of the material of component j, and m is the Weibull modulus of the material. The characteristic strength σ_0 is also the scale parameter for the distribution, while the Weibull modulus m is the shape parameter. The reference volume V_0 is related to the characteristic strength σ_0 of the material.

In our case, however, the Weibull method was slightly modified to account for the fact that the anode and cathode materials are composites made up of two different components (Ni-YSZ for the anode and LSM-YSZ for the cathode). The method employed is described next. The Weibull parameters used for the ceramic materials (LSM and YSZ) are shown in Table 4 (Laurencin et al., 2008). Only room temperature values of the Weibull parameters were used in this study.

Material	Weibull modulus, m	Characteristic strength, σ_0 (MPa)	Reference volume, V_0 (mm^3)
LSM	7.0	52.0	1.21
YSZ	7.0	446.0	0.35

Table 4. Weibull parameters of ceramic materials (room temperature values)

The results of each stress analysis case were post-processed by writing programs to extract the three principal stress values from each element in the anode and cathode FE models. These principal stresses were then used to perform a Weibull analysis to determine the probability of failure of the anode and cathode at each ΔT value. Since the SOFC component materials are subjected to a multi-axial state of stress, the total survival probability of each ceramic phase of the anode/cathode under the action of the three principal stresses (σ_1, σ_2, and σ_3) was calculated. The principal stresses were assumed to act independently, and the total survival probability was calculated as the product of the survival probabilities under the action of each individual principal stress (Laurencin et al., 2008):

$$P_s^j\left(\overline{\sigma}, V_j\right) = \prod_{i=1}^{3} P_s^j\left(\sigma_i, V_j\right) \tag{2}$$

Also,

$$P_s^j\left(\sigma_i, V_j\right) = \exp\left(-\int_{V_j}\left(\frac{\sigma_i}{\sigma_0}\right)^m \frac{dV_j}{V_0}\right) \tag{3}$$

where, j = YSZ for the anode, j = LSM or YSZ for the cathode, and i = 1, 2, and 3. Only tensile values of the three principal stresses were used in the Weibull analysis. The probability of failure of each phase was then calculated as follows (Anandakumar et al., 2010):

$$P_f = 1.0 - P_s^j\left(\overline{\sigma}, V_j\right) \tag{4}$$

The probability of failure of the anode was calculated as the failure probability of the YSZ phase, keeping in mind that the anode material is a cermet composite (Ni-YSZ), and that the Weibull distribution is more appropriate for calculating the failure probability of ceramics (such as YSZ) (Laurencin et al., 2008). The strength distribution for metals such as nickel is closer to a normal distribution (Meyers & Chawla, 1999). Since the cathode is a composite of two different ceramic materials (LSM-YSZ), the probability of failure of the cathode was calculated by extracting positive (tensile) values of the three principal stresses from each element in the LSM and YSZ element sets of the cathode FE model, and subjecting these to the Weibull analysis. This resulted in two different failure probability values for the LSM and YSZ phases of the cathode, which were combined into a single probability of failure value for the cathode by assuming that the cathode fails when either phase fails (or when both phases fail simultaneously). The probability that both phases fail simultaneously was calculated by assuming that the failures of the two phases are independent events, and hence the probability of simultaneous failure of the two phases is just the product of the probabilities of failure of LSM and YSZ:

$$P_f^{cathode} = P_f\left(LSM \cup YSZ\right)$$

$$\Rightarrow P_f^{cathode} = P_f\left(LSM\right) + P_f\left(YSZ\right) - P_f\left(LSM \cap YSZ\right)$$

$$\Rightarrow P_f^{cathode} = P_f\left(LSM\right) + P_f\left(YSZ\right) - P_f\left(LSM\right)P_f\left(YSZ\right)$$

4.2.1 Anode

The probability of failure (P_f) value for the YSZ phase of the anode was calculated at each ΔT value (100ºC, 200ºC, ..., 800ºC) for each case described in Table 1. These values are plotted in Figure 10. Since these P_f values are calculated on the basis of the tensile principal stresses in the YSZ phase, the variation of the maximum principal tensile stress (MPTS) in the YSZ phase of the anode with temperature in all three cases (temperature-independent material properties, temperature-dependent CTEs, and elastic-plastic behavior of Ni) is shown in Figure 11.

The P_f plot for the anode (Figure 10) shows that the probability of failure increases with increasing ΔT values (and hence increasing stresses), for each of the three cases considered (temperature-independent material properties, temperature-dependent CTEs, and elastic-plastic behavior of nickel). Also, the plot shows that the linear elastic material behavior models significantly underestimate the probability of failure of the anode (defined by the P_f

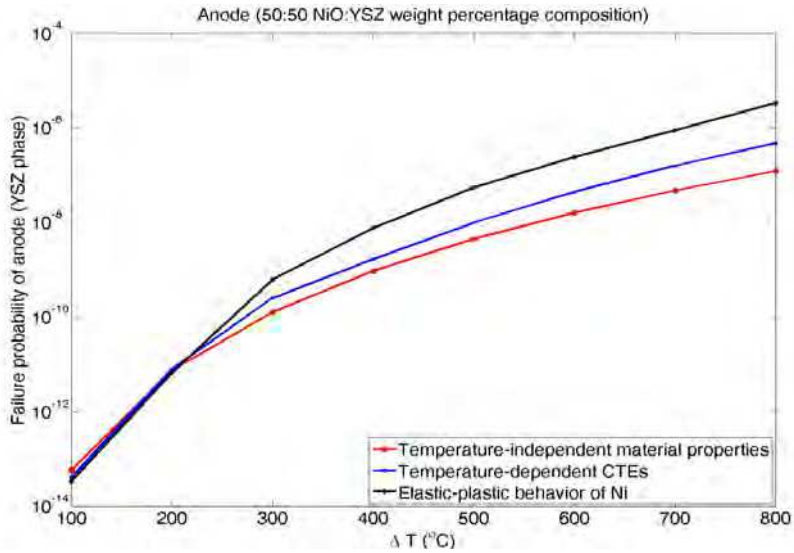

Fig. 10. Probability of failure values for anode

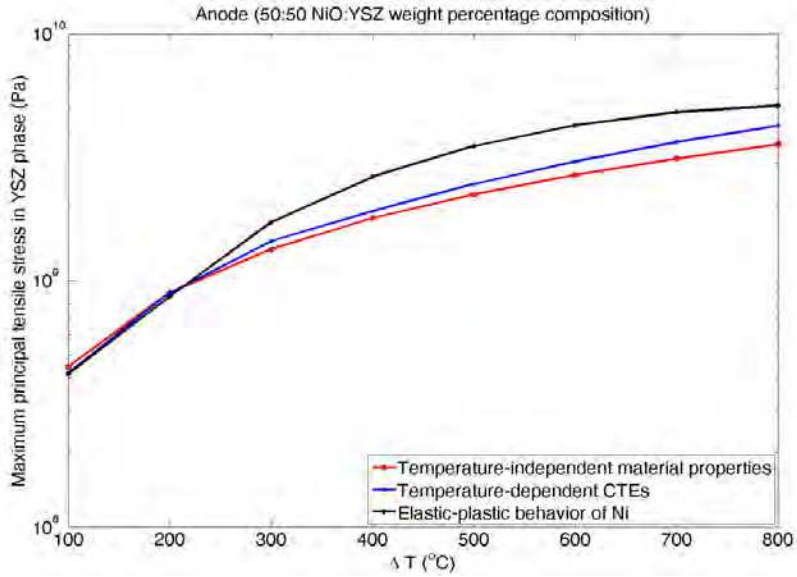

Fig. 11. Maximum principal tensile stress in the YSZ phase of the anode

values of the YSZ phase), as compared with the model that considers nonlinear elastic-plastic behavior of nickel, especially at high temperatures. This may be explained by referring to Figure 11, which shows that the maximum principal tensile stress (MPTS) in the YSZ phase of the anode increases with increasing ΔT values for all three cases, as expected. Figure 11 also shows that when the elastic-plastic behavior of Ni is taken into account, the

MPTS in the YSZ phase attains higher values than when linear elastic behavior is assumed, especially at high temperatures. This can be explained as follows: when the Ni phase enters the nonlinear (plastic) part of its stress-strain curve at higher temperatures (and hence higher strains), lower stresses are induced in the Ni phase than if its stress-strain curve had been purely linear elastic with the same value of Young's modulus. Thus, when the Ni phase starts showing nonlinear behavior, a higher proportion of the temperature-induced stresses are redistributed into the YSZ phase, resulting in higher MPTS values in the YSZ phase (and hence higher P_f values for the anode).

Figure 10 also shows that the case with temperature-dependent CTEs shows higher P_f values than the case with temperature-independent material properties at intermediate and high temperatures. Again, Figure 11 shows that with temperature-dependent CTE values, higher tensile stresses are induced in the YSZ phase of the anode than with temperature-independent material properties, especially at intermediate and high temperatures. This can be explained by referring to Figure 4, which shows that the CTEs of both Ni and YSZ increase with temperature. Since thermal stresses are proportional to CTE values, it can be expected that the case with temperature-dependent CTEs will show higher MPTS values (and hence higher P_f values) than the case with temperature-independent material properties, which uses constant (room-temperature) values of the CTEs.

4.2.2 Cathode

The probability of failure (P_f) values for the LSM and YSZ phases of the cathode were calculated and combined, as described above, at each ΔT value (100°C, 200°C, ..., 800°C) for both the cases described in Table 2. These values are plotted in Figure 12.

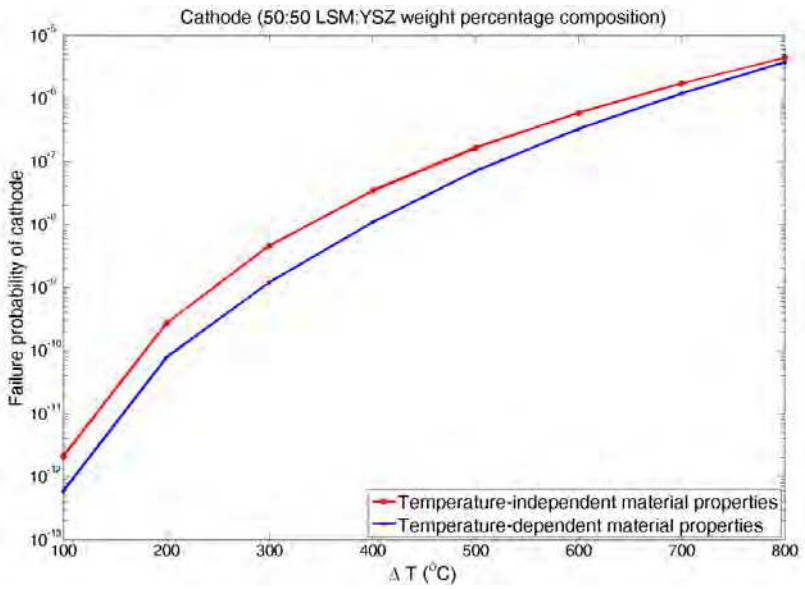

Fig. 12. Failure probability values for cathode

The P_f plot for the cathode shows that the probability of failure of the cathode increases with increasing ΔT values (and hence increasing stresses), for both temperature-independent and temperature-dependent material properties, as expected. Higher P_f values are obtained when temperature-independent material properties are considered. A physical explanation for this observation is suggested by the temperature variation of the Young's modulus of YSZ. For YSZ, E decreases from a value of 205 GPa at T = 20^0C to a value of 147.5 GPa at T = 800^0C, as shown in Figure 5. On the other hand, when temperature-independent material properties are considered, the Young's modulus of YSZ has a constant value of 205 GPa. Thus, because of the large decrease in the Young's modulus of YSZ with increasing temperature, lower stresses are induced in the cathode in the case with temperature-dependent material properties than in the case with temperature-independent material properties. This in turn leads to lower P_f values in the case with temperature-dependent material properties as compared with the case that considers temperature-independent material properties. This is confirmed by the MPTS plot for the cathode shown below (Figure 13), which compares the maximum principal tensile stress induced in the YSZ and LSM phases of the cathode for temperature-independent and temperature-dependent material properties.

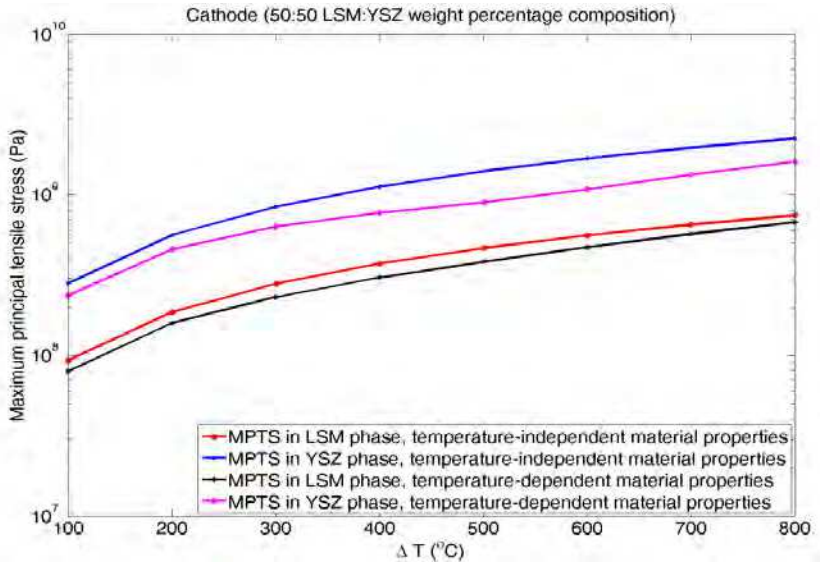

Fig. 13. Maximum principal tensile stress in LSM and YSZ phases of cathode

The plot above shows that the MPTS induced in the LSM phase for temperature-dependent material properties is lower than the MPTS in the LSM phase for temperature-independent material properties over the entire temperature range. Similarly, the MPTS induced in the YSZ phase for temperature-dependent material properties is lower than the MPTS induced in the YSZ phase for temperature-independent material properties over the entire temperature range. This implies that the cathode P_f values, which are calculated on the basis of the positive (tensile) principal stresses in the LSM and YSZ phases, will be higher for the

temperature-independent material properties case than for the temperature-dependent material properties case, as is indeed observed.

5. Conclusions

Three-dimensional FE models of SOFC anode and cathode microstructures were constructed from a stack of two-dimensional SEM images of actual cross-sections of anode and cathode microstructures. The models were subjected to spatially uniform predefined temperature fields of increasing magnitude and the resulting distribution of stresses was obtained using FEA. The obtained stresses were subjected to Weibull analyses to determine the failure probability of the anode and cathode as a function of temperature. *The novelties of this work include FE analysis of the mechanical response of microstructure-based anode and cathode models to temperature loads, consideration of temperature-dependent material properties of the anode and cathode materials, and consideration of nonlinear elastic-plastic behavior of the nickel phase of the Ni-YSZ anode*. The Weibull analyses showed that the linear elastic material models underestimate the failure probability of the anode at high temperatures; hence, it is important to consider the nonlinear behavior of the nickel phase of the Ni-YSZ anode. Also, it was found that consideration of temperature-independent material properties of the cathode materials results in higher failure probability values than those obtained with temperature-dependent material properties.

6. Acknowledgements

We acknowledge the financial support for this work from the National Science Foundation under the Faculty Early Career Development (CAREER) Grant CMMI-0546225 (Material Design & Surface Engineering Program). We also acknowledge the technical support from Dr. Scott Barnett at the Department of Materials Science and Engineering at Northwestern University who generously provided a series of 2-D SEM images of anode and cathode microstructures.

7. References

Anandakumar, G., Li, N., Verma, A., Singh, P., & Kim, J.-H. (2010). Thermal stress and probability of failure analyses of functionally graded solid oxide fuel cells. *Journal of Power Sources,* Vol. 195, (2010), pp. (6659-6670).

Atkinson, A., & Selcuk, A. (2000). Mechanical behavior of ceramic oxygen ion-conducting membranes. *Solid State Ionics,* Vol. 134, (2000), pp. (59-66).

Ebrahimi, F., Bourne, G., Kelly, M., & Matthews, T. (1999). Mechanical properties of nanocrystalline nickel produced by electrodeposition. *NanoStructured Materials*, Vol. 11, No. 3, (1999), pp. (343-350).

Giraud, S., & Canel, J. (2008). Young's modulus of some SOFCs materials as a function of temperature. *Journal of the European Ceramic Society*, Vol. 28, (2008), pp. (77-83).

Johnson, J., & Qu, J. (2008). Effective modulus and coefficient of thermal expansion of Ni-YSZ porous cermets. *Journal of Power Sources*, Vol. 181, (2008), pp. (85-92).

Kramer, J., Mastronarde, D., & McIntosh, J. (1996). Computer visualization of three-dimensional image data using IMOD. *Journal of Structural Biology*, Vol. 116, (1996), pp. (71-76).

Laurencin, J., Delette, G., Lefebvre-Joud, F., & Dupeux, M. (2008). A numerical tool to estimate SOFC mechanical degradation: case of the planar cell configuration. *Journal of the European Ceramic Society*, Vol. 28, (2008), pp. (1857-1869).

Meyers, M., & Chawla, K. (1999). *Mechanical Behavior of Materials*, Prentice Hall, ISBN 0132628171, Upper Saddle River, New Jersey.

Nakajo, A., Stiller, C., Harkegard, G., & Bolland, O. (2006). Modeling of thermal stresses and probability of survival of tubular SOFC. *Journal of Power Sources*, Vol. 158, (2006), pp. (287-294).

Pihlatie, M., Kaiser, A., & Mogensen, M. (2009). Mechanical properties of NiO/Ni-YSZ composites depending on temperature, porosity and redox cycling. *Journal of the European Ceramic Society*, Vol. 29, (2009), pp. (1657-1664).

Pitakthapanaphong, S., & Busso, E. (2005). Finite element analysis of the fracture behaviour of multi-layered systems used in solid oxide fuel cell applications. *Modelling and Simulation in Materials Science and Engineering*, Vol. 13, (2005), pp. (531-540).

Selcuk, A., & Atkinson, A. (1997). Elastic properties of ceramic oxides used in solid oxide fuel cells (SOFC). *Journal of the European Ceramic Society*, Vol. 17, (1997), pp. (1523-1532).

Selcuk, A., & Atkinson, A. (2000). Strength and toughness of tape-cast yttria-stabilized zirconia. *Journal of the American Ceramic Society*, Vol. 83, No. 8, (2000), pp. (2029-2035).

Singhal, S., & Kendall, K. (Eds.). (2003). *High Temperature Solid Oxide Fuel Cells: Fundamentals, Design and Applications*, Elsevier, ISBN 1856173879, Oxford.

Toftegaard, H., Sorensen, B., Linderoth, S., Lundberg, M., & Feih, S. (2009). Effects of heat-treatments on the mechanical strength of coated YSZ: an experimental assessment. *Journal of the American Ceramic Society*, Vol. 92, No. 11, (2009), pp. (2704-2712).

Toftegaard, H., & Sorensen, B. (2009). Effects of heat-treatments on the mechanical strength of coated YSZ: an experimental assessment. *Journal of the American Ceramic Society*, Vol. 92, No. 11, (2009), pp. (2704-2712).

Weibull, W. (1951). A statistical distribution function of wide applicability. *ASME Journal of Applied Mechanics,* (1951), pp. (293-297).

Wilson, J., Kobsiriphat, W., Mendoza, R., Chen, H.-Y., Hiller, J., Miller, D., Thornton, K., Voorhees, P., Adler, S., & Barnett, S. (2006). Three-dimensional reconstruction of a solid-oxide fuel-cell anode. *Nature Materials*, Vol. 5, (2006), pp. (541-544).

Wilson, J., & Barnett, S. (2008). Solid oxide fuel cell Ni-YSZ anodes: effect of composition on microstructure and performance. *Electrochemical and Solid-State Letters,* Vol. 11, No. 10, (2008), pp. (B181-B185).

Wilson, J., Duong, A., Gameiro, M., Chen, H.-Y., Thornton, K., Mumm, D., & Barnett, S. (2009). Quantitative three-dimensional microstructure of a solid oxide fuel cell cathode. *Electrochemistry Communications,* Vol. 11, (2009), pp. (1052-1056).

Xiao, C., Mirshams, R., Whang, S., & Yin, W. (2001). Tensile behavior and fracture in nickel and carbon doped nanocrystalline nickel. *Materials Science and Engineering A*, Vol. 301, (2001), pp. (35-43).

Zhang, T., Zhu, Q., Huang, W., Xie, Z., & Xin, X. (2008). Stress field and failure probability analysis for the single cell of planar solid oxide fuel cells. *Journal of Power Sources*, Vol. 182, (2008), pp. (540-545).

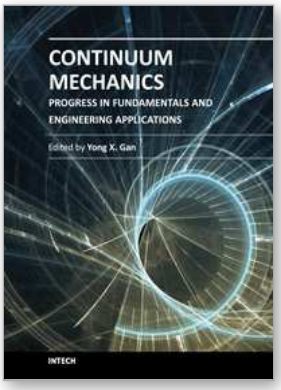

Continuum Mechanics - Progress in Fundamentals and Engineering Applications

Edited by Dr. Yong Gan

ISBN 978-953-51-0447-6
Hard cover, 158 pages
Publisher InTech
Published online 28, March, 2012
Published in print edition March, 2012

Continuum Mechanics is the foundation for Applied Mechanics. There are numerous books on Continuum Mechanics with the main focus on the macroscale mechanical behavior of materials. Unlike classical Continuum Mechanics books, this book summarizes the advances of Continuum Mechanics in several defined areas. Emphasis is placed on the application aspect. The applications described in the book cover energy materials and systems (fuel cell materials and electrodes), materials removal, and mechanical response/deformation of structural components including plates, pipelines etc. Researchers from different fields should be benefited from reading the mechanics approached to real engineering problems.

How to reference

In order to correctly reference this scholarly work, feel free to copy and paste the following:

Sushrut Vaidya and Jeong-Ho Kim (2012). Continuum Mechanics of Solid Oxide Fuel Cells Using Three-Dimensional Reconstructed Microstructures, Continuum Mechanics - Progress in Fundamentals and Engineering Applications, Dr. Yong Gan (Ed.), ISBN: 978-953-51-0447-6, InTech, Available from: http://www.intechopen.com/books/continuum-mechanics-progress-in-fundamentals-and-engineering-applications/continuum-mechanics-of-solid-oxide-fuel-cells-using-three-dimensional-reconstructed-microstructures

INTECH
open science | open minds

InTech Europe
University Campus STeP Ri
Slavka Krautzeka 83/A
51000 Rijeka, Croatia
Phone: +385 (51) 770 447
Fax: +385 (51) 686 166
www.intechopen.com

InTech China
Unit 405, Office Block, Hotel Equatorial Shanghai
No.65, Yan An Road (West), Shanghai, 200040, China
中国上海市延安西路65号上海国际贵都大饭店办公楼405单元
Phone: +86-21-62489820
Fax: +86-21-62489821